

# Optimization of array encoding for ultrasound imaging

**Jacob Spainhour<sup>1</sup>, Korben Smart<sup>2</sup>, Stephen Becker<sup>1</sup> and Nick Bottenus<sup>3</sup>**

<sup>1</sup> Department of Applied Mathematics, University of Colorado Boulder, USA

<sup>2</sup> Department of Physics, University of Colorado Boulder, USA

<sup>3</sup> Paul M. Rady Department of Mechanical Engineering, University of Colorado Boulder, USA

E-mail: [Jacob.Spainhour@colorado.edu](mailto:Jacob.Spainhour@colorado.edu), [Korben.Smart@colorado.edu](mailto:Korben.Smart@colorado.edu),  
[Stephen.Becker@colorado.edu](mailto:Stephen.Becker@colorado.edu), [Nick.Bottenus@colorado.edu](mailto:Nick.Bottenus@colorado.edu)

**Abstract.**

*Objective:* The transmit encoding model for synthetic aperture imaging is a robust and flexible framework for understanding the effect of acoustic transmission on ultrasound image reconstruction. Our objective is to use machine learning (ML) to construct scanning sequences, parameterized by time delays and apodization weights, that produce high quality B-mode images.

*Approach:* We use an ML model in PyTorch and simulated RF data from Field II to probe the space of possible encoding sequences for those that minimize a loss function that describes image quality. This approach is made computationally feasible by a novel formulation of the derivative for delay-and-sum beamforming. We demonstrate these results experimentally on wire targets and a tissue-mimicking phantom.

*Main Results:* When trained according to a given set of imaging parameters (imaging domain, hardware restrictions), our ML imaging model produces optimized encoding sequences that improve a number of standard quality metrics including resolution, field of view, and contrast, over conventional sequences.

*Significance:* This work demonstrates that the set of encoding schemes that are commonly used represent only a narrow subset of those available. Additionally, it demonstrates the value for ML tasks in synthetic transmit aperture imaging to consider the beamformer within the model, instead of as purely post-processing.

*Keywords:* synthetic aperture, spatial encoding, numerical optimization, machine learning, image quality

**1. Introduction**

In classical ultrasound imaging, transmissions from a transducer array are focused towards specific locations in the target medium, and the backscattered echoes are collected and processed into an image that is clear at these locations (Cobbold, 2007). More modern systems use a synthetic transmit aperture system that combines the echoes from multiple transmissions to recreate this focus across multiple points in the region. In the ideal case, these transmissions are produced by firing each array element individually in sequence and combining the full set of element-to-element signals into a B-mode image that achieves focus even at depth (Jensen et al., 2006). However, the large number of transmissions needed paired with the relatively low power of each means that, when performed directly, this procedure creates images with poor frame rate and low signal-to-noise ratio (SNR), making it impractical for clinical application (Chiao et al., 1997).

Retrospective Encoding For Conventional Ultrasound Sequences, or REFoCUS, is an alternative approach that considers the responses from an *arbitrary* transmission as a linear combination of these pairwise element responses (Ali et al., 2020; Bottenus, 2018). In this way, the transmission sequence of time delays and apodization weights parameterizes an *encoding* of the ground truth basis of element-to-element signals, the multistatic (STA) data set. By leveraging properties of the specific sequence used, the echoed response signals can then be *decoded* to produce a robust approximation of this basis. This approximation can then be focused throughout the imaging domain as post-processing, making a B-mode image that achieves the desired SNR and focal

depth. Conventional transmission sequences are often selected according to geometric principles (e.g., focused, plane wave, or diverging beams) or according to spatial codes (e.g., Hadamard (Chiao et al., 1997) or S-sequence (Harrison et al., 2014)). However, the REFoCUS framework generalizes this encoding to allow for a uniform treatment of other categories of transmissions (Bottenus et al., 2023).

The quality of the resultant B-mode image—measured in terms of resolution, field of view (FOV), and artifacts—is highly dependent on properties of the transmit sequence. As an example of the importance of beam geometry, focused beams provide very high resolution, but only at or around a particular focal point. One of the most influential properties is simply the number of transmissions. Ideally, the number of transmissions matches or exceeds the number of array elements. While such a choice would (in principle) minimize information loss during encoding and decoding, practical frame rate considerations often restrict this. However, it is still possible to reduce information loss in the more general, underdetermined case. Some groups have shown success using randomly assigned delays, as such schemes lead to very well conditioned, and therefore stably invertible, encoding matrices (You et al., 2021). Similarly, a spatial code for element apodizations can often be applied to produce a lossless encoding (or near-lossless when the matrix must be truncated (Zhang et al., 2022)), which in turn increases SNR during imaging.

However, the space of all possible encoding sequences dwarfs those immediately clear and desirable properties (Spainhour et al., 2022). In this paper, we present a novel machine learning (ML) architecture that can efficiently search the set of possible transmit sequences to identify those whose response echoes lead to high quality images using the REFoCUS encoding framework. When trained according a specific set of imaging parameters and hardware restrictions, these machine learning models produce *optimized* sequences that realize image quality beyond what is attainable through conventional transmit sequences. In doing so, we show that there exist notable counterexamples to the principle that a better conditioned encoding leads to higher quality images. This motivates us to design an ML architecture that measures quality of a sequence *after* image formation, reflecting how performance is judged in a clinical setting.

Techniques in machine learning have gained a significant amount of research attention in the field of ultrasound imaging, particularly in the application of deep learning and neural networks (Hyun et al., 2021; Liu et al., 2019). Following the unprecedented successes of the deep convolutional neural network AlexNet in non-medical imaging tasks (Krizhevsky et al., 2017), similar networks are often trained and utilized for ultrasound-adjacent tasks as an additional post-processing step to a conventional imaging pipeline, performing classification, segmentation, etc. on image data (Mischi et al., 2020).

Other ML approaches are concerned with image formation more directly. In a prototypical setup, a deep neural network is fed the received echoes of a transducer array and produces a B-mode image, aiding or even supplanting the use of a conventional

beamformer (van Sloun et al., 2020). Often the goal in such cases is to create a network that can be evaluated faster than the analogous classical imaging process with no discernible loss in image quality. Other times, this network can also be designed to directly *improve* image quality. For example, Hyun et al. (2019) utilize a deep CNN as a beamformer that reduces speckle, citing considerable advantages over conventional delay-and-sum techniques.

In contrast, the proposed machine learning architecture seeks to improve imaging quality through influencing data *acquisition* through optimization of the encoding sequence. In particular, this means our ML model parameters have a direct, physical interpretation, with each parameterization corresponding to a particular set of transmissions by the transducer array. Once an optimized encoding sequence has been found, reconstructing an image from the resulting data can be done using classical techniques without further reference to the ML model itself. In this way the proposed framework avoids the inherent intractability of a standard neural network architecture, where model parameters such as weights and biases have meaning only within the context of the ML model itself.

An adjacent strategy to our own is employed by Chen et al. (2021), in which a stacked denoising autoencoder is used to train pulse-inverted apodization weights (+1/−1) of plane wave transmissions, the first layer of which are the weights themselves. Their ML model is trained to optimize the reconstruction of the multistatic data set, and boasts higher image quality with a smaller computation time. In our approach, we allow even further control of the sequence through a fully continuous treatment of apodization weights *and* time delays within the ML model, with no other trainable parameters. This approach to ML architecture has both theoretical and practical advantages. First and foremost, this means that a fully trained ML model of our kind is immediately interpretable in a way that is not possible for a deep neural network, as the parameters directly represent the inputs passed to a physical ultrasound array, which lends them to further study and discovery. As we will show, this also makes the optimized encoding sequence useful well beyond our training data, as the sequence has been generated in accordance with more general acoustic principles. Furthermore, this smaller parameter space dramatically reduces the training time needed to generate an optimized encoding sequence. This allows for greater flexibility in usage, as an ML model in our framework can be retrained at a minimal cost when the experimental setting changes.

## 2. Methods

### 2.1. Transmit Encoding Theory

We consider a linear transducer array of  $N_E$  physical elements. Each element performs at least one of two functions:  $N_T$  of them transmit a diverging wave, and  $N_R$  of them receive backscattered echoes. While there is flexibility in which array elements perform which task, it is typical to have each act as both receive and transmit elements, such that

$N_T = N_R = N_E$ . Collected across all pairs of transmit and receive elements, these signals form a time dependent  $N_T \times N_R$  matrix  $\mathbf{U}(t)$ , within which the matrix element  $u_{TR}(t)$  is the signal observed by transmitting on element  $T$  and receiving on element  $R$ . In the synthetic transmit aperture model, the complete collection of pulse-echo response signals between pairs of transmit and receive elements make up the multistatic data set. Because these signals can be delayed and summed across the receive channel to produce transmit focus throughout the domain, as in Delay-and-Sum (DAS) imaging, these data can be considered the mathematical basis of our imaging (Jensen et al., 2006).

As discussed in the introduction, it is technically possible, although practically inadvisable, to construct  $\mathbf{U}(t)$  directly by firing each transmit element in sequence across a total of  $N_T$  transmissions (Chiao et al., 1997). Instead, the REFOCUS technique seeks to construct an approximation of  $\mathbf{U}(t)$  using the responses from either a conventional set of transmissions, such as those that produce focused beams, or more arbitrary scanning sequences by allowing for flexibility of time delays and apodization (Ali et al., 2020).

In either case, we consider there to be a total of  $N_M$  separate transmissions, each of which is parameterized by  $N_T$  time delays  $t_{MT}$  and apodization weights  $w_{MT}$ . The response observed by receive element  $R$  from transmit  $M$  can be described as a weighted sum of time delayed matrix elements from the multistatic data set,

$$s_{MR}(t) = \sum_{T=1}^{N_T} w_{MT} u_{TR}(t - t_{MT}), \quad (1)$$

which are similarly collected into a time dependent  $N_M \times N_R$  matrix  $\mathbf{S}(t)$  of focused responses. Collected across each transmit, these time delays and apodization weights make up the *encoding sequence*, denoted  $\boldsymbol{\sigma} = (t, w)_{MT}$ .

It is now convenient to work in the frequency domain, where each time delay of  $u_{TR}(t)$  becomes a complex phase shift of  $u_{TR}(\omega)$  (Ali et al., 2020). For simplicity, we represent the frequency dependent Fourier transform of  $\mathbf{U}(t)$  and  $\mathbf{S}(t)$  as  $\mathbf{U}(\omega)$  and  $\mathbf{S}(\omega)$  respectively. In doing so, we can express the transmission response of receive element  $R$  to transmission  $M$  as

$$s_{MR}(\omega) = \sum_{T=1}^{N_T} w_{MT} \exp(-j\omega t_{MT}) u_{TR}(\omega). \quad (2)$$

This describes a linear relationship between the multistatic data set  $\mathbf{U}(\omega)$  and the transmission responses  $\mathbf{S}(\omega)$  that is fully parameterized by  $\boldsymbol{\sigma}$ , given by

$$\mathbf{S}(\omega) = \mathbf{H}(\omega) \mathbf{U}(\omega), \quad (3)$$

where  $\mathbf{H}(\omega)$  is a frequency dependent  $N_M \times N_T$  *encoding matrix* given by

$$\mathbf{H}(\omega) = \begin{bmatrix} w_{1,1} \exp(-j\omega t_{1,1}) & \dots & w_{1,T} \exp(j\omega t_{1,T}) \\ w_{2,1} \exp(-j\omega t_{2,1}) & \dots & w_{2,T} \exp(j\omega t_{2,T}) \\ \vdots & \ddots & \vdots \\ w_{M,1} \exp(-j\omega t_{M,1}) & \dots & w_{M,T} \exp(j\omega t_{M,T}) \end{bmatrix}. \quad (4)$$

In practice, we collect only discrete, equispaced samples from  $\mathbf{S}(t)$ , from which we have a total of  $N_\omega$  angular frequencies  $\omega$ . Because calculations involving the collection of matrices  $\mathbf{S}(\omega)$  are typically performed in parallel across frequencies, we use calligraphic letters to denote the collection of all frequencies. As an example, we denote  $\mathcal{S}_\omega = \mathbf{S}(\omega)$ , and represent the above equation more compactly as  $\mathcal{S} = \mathcal{H}\mathcal{U}$ . When we wish to emphasize the dependence of our encoding matrices  $\mathcal{H}$  on the sequence  $\sigma$ , we add  $\sigma$  as a subscript.

The objective of the REFoCUS framework is to create an approximation of the multistatic data set  $\hat{\mathcal{U}}$  from the recorded echoes in  $\mathcal{S}$ . This is done by applying a frequency dependent *decoder*  $\mathbf{H}^\dagger(\omega)$  to  $\mathbf{S}(\omega)$ , resulting in

$$\hat{\mathcal{U}} = \mathcal{H}^\dagger \mathcal{S} = (\mathcal{H}^\dagger \mathcal{H}) \mathcal{U}. \quad (5)$$

This decoder is in principle arbitrary, with possible options ranging from a per-frequency conjugate transpose (Bottenus, 2018) to a fully trained neural network (Chen et al., 2021). In this work, we follow Ali et al. (2020); Bottenus et al. (2023) and apply a Tikhonov regularized pseudoinverse that has been shown to work well experimentally. This choice of decoder depends only on the original encoding matrix, which is again dependent only on our sequence  $\sigma$ . The Tikhonov decoder is given explicitly by

$$\mathcal{H}^\dagger = (\mathcal{H}^* \mathcal{H} + \gamma^2 \mathcal{I}_{N_E})^{-1} \mathcal{H}^*, \quad (6)$$

where  $\mathcal{H}^*$  is the conjugate transpose of  $\mathcal{H}$  and  $\gamma$  is a regularization constant. This regularization serves to suppress the contribution of noise to the recovered multistatic channel data, but also to produce a better conditioned inversion of  $\mathcal{H}$ . Together, this results in a more accurate, stable recovery of  $\hat{\mathcal{U}}$ . This is particularly important in the underdetermined system of interest, in which the number of transmits  $N_M$  is significantly smaller than the number of array elements  $N_E$ . In all usages of regularization herein we take a value of  $\gamma = 0.1\sigma_{\max}(\omega)$ , where  $\sigma_{\max}(\omega)$  is the spectral norm of each per-frequency encoding matrix  $\mathbf{H}(\omega)$ . This particular value has been observed empirically to avoid issues of over- or under-regularization in the presence of noise (Bottenus et al., 2023).

## 2.2. Beamforming and Imaging Procedure

Given a multistatic data set  $\mathcal{U}$ , we can produce the 2D B-mode image of interest using conventional DAS beamforming. This technique maps the multistatic IQ data (either the ground truth or approximated) at each frequency to a single IQ data matrix, taking a sum of the time delayed data in  $\hat{\mathcal{U}}$ . By manipulating these post-acquisition time delays, an image is created that is focused at arbitrary points in the imaging domain, in this case individual pixels. Mathematically, we denote this beamforming operation as  $\mathcal{B} : \mathbb{C}^{N_M \times N_R \times N_\omega} \rightarrow \mathbb{C}^{N_x \times N_z}$ , where  $(N_x, N_z)$  are the number of pixels in the lateral and axial directions of our image.

To complete our description of the imaging process, we apply to this re-focused IQ data a number of post-processing steps that make the resulting image suitable

for interpretation by a human observer. These include the computation of the signal envelope, log-scaling the dynamic range, and clipping the image to a minimum decibel value. In our notation, we choose to represent these operations collectively as  $|\cdot|_{\text{Im}} : \mathbb{C}^{N_x \times N_z} \rightarrow \mathbb{R}^{N_x \times N_z}$ . Altogether, this means that given a set of  $N_M$  transmission responses collected in  $\mathbf{S}$  and an encoding sequence  $\boldsymbol{\sigma}$ , the output of our ML model is an image represented by the real matrix  $|\mathcal{B}(\mathcal{H}_\sigma^\dagger \mathbf{S})|_{\text{Im}}$ .

Ultimately, our objective is to design an ML model that is trained to generate high-quality encoding sequences for a given imaging configuration. In doing so, it is important that we define “high-quality” to correlate with usefulness in a clinical setting, which we will show is a distinct goal from simply optimizing the recovery of  $\mathbf{U}$  from  $\mathbf{S}$ . There is ongoing discussion in the beamforming literature about how to properly evaluate generated B-mode images (Dei et al., 2017; Long et al., 2018; Ranganathan and Walker, 2007), and recently much of this discussion exists in the context of improving evaluation metrics for ML models (Hyun, 2022).

In this work, we define for our ML model an arbitrary *loss function*  $\mathcal{L} : \mathbb{R}^{N_x \times N_z} \rightarrow \mathbb{R}^+$  that in some way measures image quality. There is much flexibility in the specific choice of loss function, but ideally we can choose one for which a lower value corresponds to higher resolution, higher SNR, wider FOV, fewer artifacts, etc. For example, a natural and easily implementable choice is a normalized  $\ell^2$  comparison to a reference image that has these desired qualities. With a given image  $\widehat{\mathbf{X}}$  and reference image  $\mathbf{X}$ , this loss is then defined by

$$\mathcal{L}_{\ell^2}(\widehat{\mathbf{X}}; \mathbf{X}) := \frac{1}{N_x N_z} \|\mathbf{X} - \widehat{\mathbf{X}}\|_2^2. \quad (7)$$

Loss functions that more directly assess the signal or image reconstruction are also possible. Many of these lead naturally to unsupervised learning during training, such as those that measure coherence of channel data or entropy of the image (Noda et al., 2020). When regions of interest for the image can be determined for the training set, loss functions that directly measure contrast become available. For example, the generalized contrast to noise ratio (gCNR) is a measure of histogram overlap between the brightness of predefined speckle and anechoic regions, such that a higher value indicates greater contrast in the image. In particular, gCNR is robust to scaling of the dynamic range, and therefore artificial increases of lesion detectability in a system (Rodriguez-Molares et al., 2019). This means that gCNR is important in evaluating the performance of an encoding sequence, and we can in principle improve it by minimizing the loss function

$$\mathcal{L}_{\text{gCNR}}(\widehat{\mathbf{X}}) := 1 - \text{gCNR}(\widehat{\mathbf{X}}), \quad (8)$$

However, complications with implementation make this loss function relatively impractical. In particular, the histogram operator is not differentiable, and standard continuous approximations are unstable. This makes the operator largely incompatible with backpropagation during the training of our ML model. In this respect, there is a clear advantage to training our ML model with  $\mathcal{L}_{\ell^2}$  over  $\mathcal{L}_{\text{gCNR}}$ , and we will show that doing so still makes a meaningful improvement to the gCNR of produced images.

### 2.3. Implementation of the Machine Learning Model

We define an optimized encoding sequence  $\sigma^*$  as one that, for a given loss function  $\mathcal{L}$ , beamformer  $\mathcal{B}$ , and decoder  $\mathcal{H}_\sigma^\dagger$ , minimizes the non-convex optimization problem

$$\min_{\sigma \in \Sigma} \mathbb{E} \mathcal{L} (|\mathcal{B}(\mathcal{H}_\sigma^\dagger \mathcal{S})|_{\text{Im}}) , \quad (9)$$

where this expectation is taken over all possible transmission responses  $\mathcal{S}$ . As it is impossible to evaluate this expectation directly, we instead consider the minimization problem as in machine learning, where we instead approximate the intractable domain with a representative sample of training data  $\{\mathcal{U}_i\}$ . Given this ground truth, each piece of data is related to a transmission response by our sequence-dependent encoding matrix  $\mathcal{H}_\sigma$  by  $\mathcal{S}_i = \mathcal{H}_\sigma \mathcal{U}_i$ . Similarly, we must restrict the space of encoding sequences to those that are practically realizable on a physical system, which we denote as  $\Sigma$ . Generally, this adds a constraint on the set of apodization weights  $\{w_{MT}\}$  that limits the total transmission power of the emitted beams. We accomplish this with a restriction to an  $\ell^\infty$  ball, effectively clipping each apodization weight to the range  $[-1, 1]$ . In the absence of such a constraint, the optimized weights would grow arbitrarily in order to artificially increase brightness, which is not possible on a realistic system. Other restrictions stem from quantization of numerical values to match machine clock cycles, which are much more dependent on the specific acquisition system and less impactful to the trained result.

Altogether, we are left to solve

$$\sigma^* = \arg \min_{\sigma \in \Sigma} \frac{1}{N_U} \sum_{i=1}^{N_U} \mathcal{L} (|\mathcal{B}(\mathcal{H}_\sigma^\dagger \mathcal{H}_\sigma \mathcal{U}_i)|_{\text{Im}}) . \quad (10)$$

Numerically, we solve Equation 10 with PyTorch, a Python package for building deep learning and other machine learning models (Paszke et al., 2019). Although we treat this problem with standard ML techniques for supervised learning, the proposed architecture is distinct from a typical deep learning approach in that the only trainable parameters are those described by the encoding sequence  $\sigma$ , altogether lacking the abstract layers of a neural network. Instead, the propagation of information through our imaging model occurs only through physically motivated operations, namely the encoding/decoding of the multistatic data and the generation of a B-mode image with DAS beamforming. Nevertheless, we mirror conventional ML approaches in that we minimize our loss function over the training data using PyTorch to backpropagate changes to the encoding sequence that most improve performance on our loss function. We perform the numerical optimization using the Adam algorithm, an adaptive version of standard stochastic gradient descent, as implemented in PyTorch (Kingma and Ba, 2017). To effectively update the parameters of the ML model requires knowledge of first order derivatives, which we obtain using the backpropagation, or reverse-mode automatic differentiation, capabilities of PyTorch. To accommodate the constraint



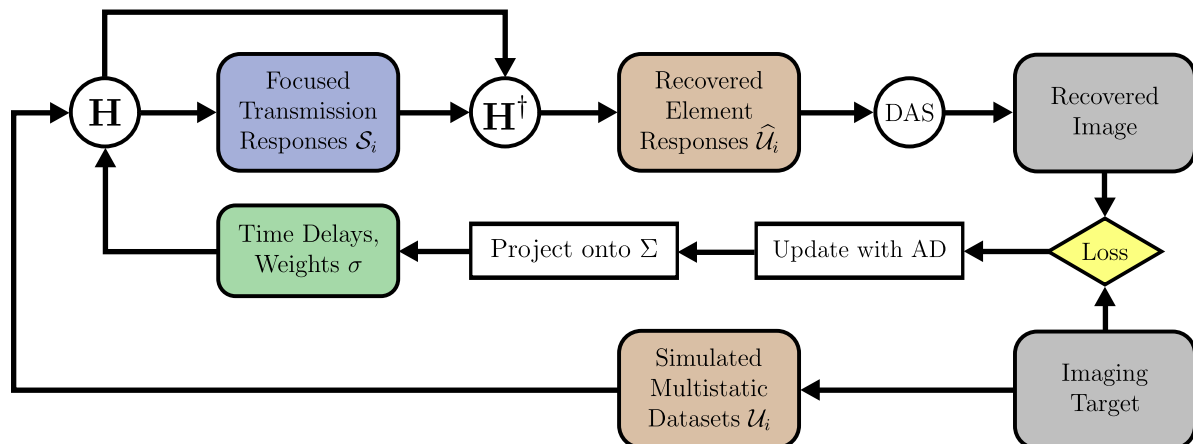


Figure 1: The training procedure for generating optimized encoding sequences. The simulated multistatic training data is encoded and decoded according to our model parameters, and an image is formed from the recovery using delay-and-sum beamforming. Depending on the nature of the loss function, the recovered B-mode image is evaluated by comparison to a target image, or with some other data obtained during the simulation, i.e. target position.

set  $\Sigma$  for physically realizable encoding sequences, we perform a simple projection of our sequence during each update. The update loop of our ML model is depicted in Figure 1.

While backpropagation is the de facto standard in deep learning applications, the more general use of automatic differentiation (AD) for optimization problems has recently gained a significant amount of attention in the field of ultrasound. Such AD tools work by directly analyzing the source code of the ML model, considering its forward execution as a composition of simple computational primitives, i.e. addition and multiplication. Derivatives of this composition can then be constructed through the chain rule using known analytic formulae. For reverse-mode AD, this allows for computations of derivatives for arbitrary functions with an upper bound of at most  $4 \times$  computational complexity (Griewank and Walther, 2008).

This computational efficiency comes at the cost of extra memory usage, which has no analogous upper bound. This is because in reverse mode AD, the number of intermediate values that must be stored increases quickly with function complexity. Machine learning software packages like PyTorch mitigate these memory concerns by including built-in analytic derivatives for more complicated, yet commonly used operators such as interpolation and discrete Fourier transforms. In the context of our ultrasound imaging model however, a direct implementation of the beamformer (a sum of linear interpolations of IQ data into per-pixel focused channel data) remains problematic during backpropagation. Regardless of how efficient evaluation of the beamformer is during the forward pass of the ML model, unwinding this large composition of operations naively is a computational bottleneck. This complication is uniquely relevant for our ML architecture, as effective optimization requires simultaneously performing these expensive calculations for entire batches of training data. As a contrasting example, the problem of shape estimation for a flexible ultrasound array has benefited considerably

from use of TensorFlow’s built-in backpropagation capabilities, as the optimization is performed only on a single piece of data concurrently (Noda et al., 2020).

In our application, we avoid this complication with a novel implementation of the derivative of the DAS beamforming operator  $\mathcal{B}$  directly in PyTorch using the exact analytical gradient. We are able to do this because the beamformed image  $\mathcal{I}$  is linear as a function of the multistatic data  $\mathcal{U}$  (Perrot et al., 2021), meaning that the Jacobian needed by PyTorch to perform the backpropagation is simply equal to its adjoint. By providing PyTorch with a method to apply this DAS adjoint to an arbitrary vector, we are able to compute this segment of the backpropagation in comparable time to the forward operation, and the additional memory overhead is eliminated altogether.

While the DAS beamforming matrix can, in principle, be constructed directly and then transposed, the size of any meaningful multistatic data set makes this practically impossible even using sparse matrices. Instead, we apply the adjoint “matrix-free,” recognizing that  $\mathcal{B}$  can be described as a sum of linear interpolations, or

$$\mathcal{B}(\mathcal{U}) = \text{Sum}(\text{Interpolate}(\mathcal{U})).$$

From this, we derive from simple analytic formulas that

$$\mathcal{B}^*(\mathcal{I}) = \text{Interpolate}^*(\text{Sum}^*(\mathcal{I})).$$

These two component adjoints have known, albeit obscure formulas (Claerbout, 2014), and so we provide pseudocode for both operations for clarity.

---

**Algorithm 1: DAS Beamformer  $\mathcal{B}$** 


---

**Input:**  $\mathcal{U}$ : Multistatic Data

**Output:**  $\mathcal{I}$ : Beamformed Image

- 1 Initialize focused IQ data at each pixel to zero
  - 2 **for** each transmit-receive element pair **do**
    - 3     /\* Linearly interpolate per-pixel time delays onto the channel data for the transmit-receive element pair     \*/
    - 4     **for** each pixel in the image **do**
    - 5         Identify the pair of IQ data the pixel focused time delay is between.
    - 6         Add a linear combination of these two IQ data to the focused IQ data
- 

#### 2.4. Acquisition of Training Data

Ideally, the ML model would be trained on true *in vivo* data of the kind of tissue of clinical interest. However, even if a large enough collection of *in vivo* data to train this model could be procured, suitable ground truth references for this data is simply unavailable by its very nature, a common problem in ultrasound ML applications (Liu

**Algorithm 2:** DAS Beamformer Adjoint  $\mathcal{B}^*$ **Input:**  $\tilde{\mathcal{I}}$ : Data of the same shape as  $\mathcal{I}$ **Output:**  $\tilde{\mathcal{U}}$ : Data of the same shape as  $\mathcal{U}$ 


---

```

1 Initialize output to zeros
2 for each transmit-receive element pair do
    /* Perform adjoint-interpolation of  $\tilde{\mathcal{I}}$  based on per-pixel time
       delays                                     */
3
4   for each pixel in the image do
5     Identify pair of IQ data the pixel focused time delay is between
6     To each index of the output where the closest pair is located, add the
       corresponding value of the linear combination in Algorithm 1

```

---

et al., 2019). As a result, we utilize simulated multistatic data to train our model. We generate this data with Field II (Jensen, 1996) using the transducer configuration described in Table 1. Although it is necessarily less complex than *in vivo* data, the quality of a particular encoding sequence can be effectively characterized by performance on different types of simulated data. For example, isolated point scatterers distributed throughout an anechoic field can be used to model the point spread function induced by a particular imaging system (Ranganathan and Walker, 2007). By greatly increasing the density of scatterers in the field, one can generate a realization of background speckle within which anechoic cysts can be placed. Such data is a valuable tool for measuring contrast and lesion detectability of an imaging system (Dei et al., 2017; Rodriguez-Molares et al., 2019).

With this kind of simulated data, there are two natural choices for the imaging target used by the loss function in Equation 7 used during the supervised learning. The first is comparison to an “unencoded” image, where each simulated, ground-truth multistatic data set is directly focused with DAS beamforming. The second is comparison to an “idealized” target that instead represents the ground-truth echogenicity. In Figure 2(a) we show an example of each of these categories of data

Parameters	Simulated array
Element count	64
Element pitch	0.3 mm
Element kerf	0.01 mm
Center frequency	3 MHz
Bandwidth	70%

Table 1: Simulated Field II Transducer Parameters

and the associated imaging target types.

Although there is inherent flexibility in target type, it is critically important that our ML model does not overfit to any particular class of synthetic training data. Instead, the optimized encoding sequence that parameterizes the ML model should improve image quality according to more general acoustic principles. Our primary method of encouraging this kind of quality involves training with anechoic lesions in an underdeveloped speckle pattern. Unlike with standard background speckle, this ensures that the loss function is capable of distinguishing individual scatterers, and is therefore more effective at reducing the point spread function throughout the viewing window. This is particularly relevant in a comparison to the ground truth echogenicity, as this encourages complete suppression of side-lobes throughout the imaging domain. In furtherance of this, we also expand the viewing window during training to slightly beyond the final targeted range to ensure that these side-lobe artifacts are completely suppressed even for scatterers on the edge of the viewing domain (See Section 4.2). Altogether, these characteristics make the ground truth contrast for anechoic lesions in a low-density speckle effective training targets, as emphasized in Figure 2(a). We generate with Field II a collection of 500 instances of such data, of which 80% form the training set and 20% form a testing set.

Furthermore, we can evaluate transmit sequences on more complex multistatic data sets generated with Field II. We follow a procedure similar to Hyun et al. (2019) and generate arrangements of scatterers with amplitudes weighted according a more variable ground truth echogenicity. These contrast maps are derived from a set of 160 images from the publicly available validation set of an ImageNet competition (Howard et al., 2018). To create these “image-derived” data, we first extract and smooth the middle  $256 \times 256$  pixels from each image and convert them to grayscale. Histogram matching is then applied to each so that when the resulting B-mode image is scaled to the appropriate dynamic range, it features a uniform distribution of brightness. This normalizes the data such that artificial improvements in the loss function cannot be achieved by simply scaling the dynamic range. The pixel values of each contrast map are then interpolated as an amplitude of nearby scatterers that are distributed throughout the spatial domain. We can also use these contrast maps to generate anechoic regions in background speckle that are more arbitrary than standard circular cysts. We do this by completely removing scatterers with an amplitude below some threshold. These data are important, as they still allow for measures of lesion detectability like gCNR. In Figure 2 we show an example of both types of imaging target—an unencoded B-mode image and the ground truth echogenicity—for each category of data.

### 2.5. Data Availability

The full code used to perform the optimization, along with the data that support the findings of this study, is openly available in the latest release of an open source GitHub repository at [github.com/jcs15c/optimal\\_ultrasound\\_encoding](https://github.com/jcs15c/optimal_ultrasound_encoding).

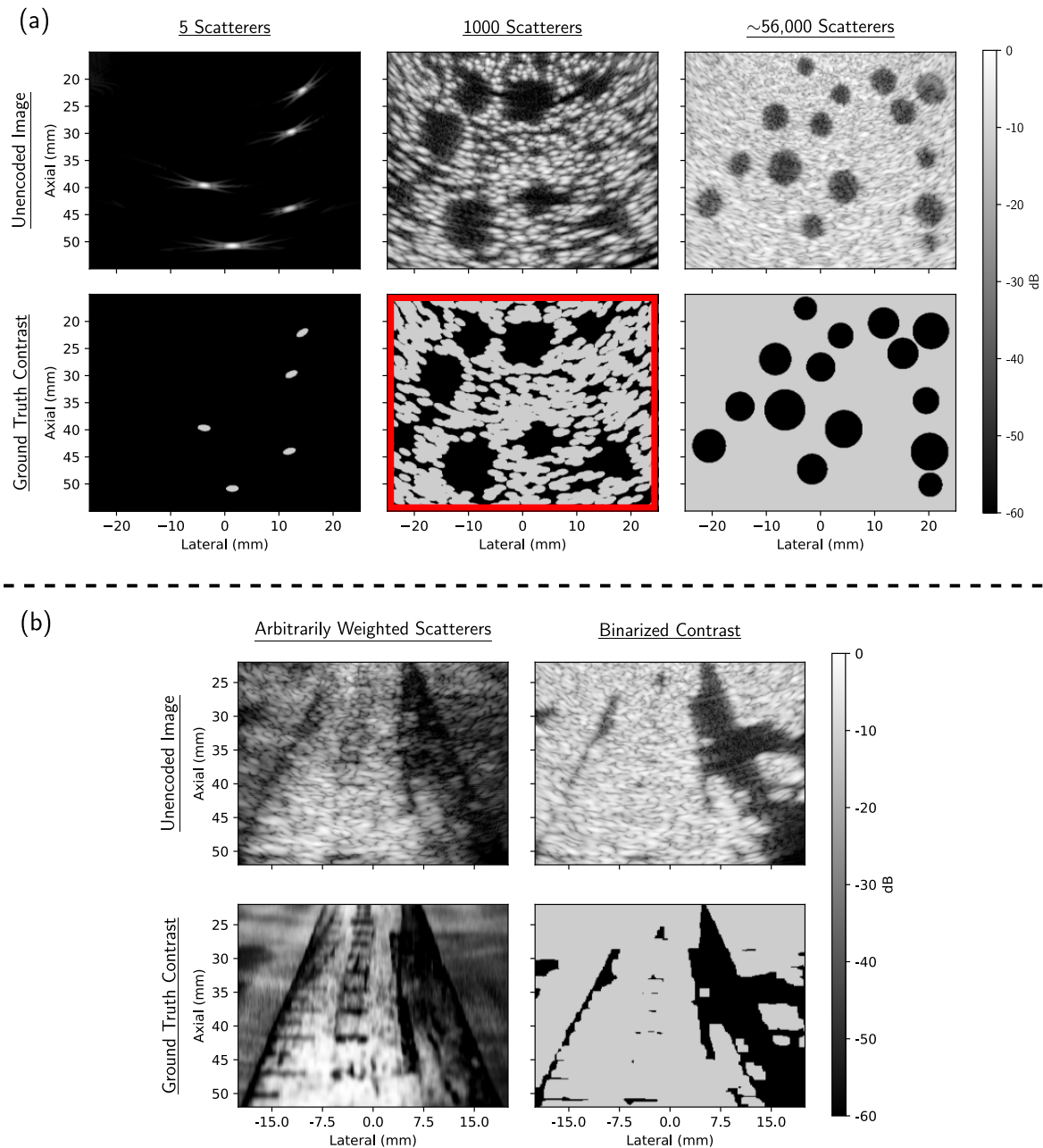


Figure 2: The various types of simulated data and imaging target type on which the ML model is trained and/or evaluated. (a) Typical imaging targets generated from the responses of individual scatterers in an anechoic field. With these we can depict isolated point targets (left) or anechoic lesions in a realization of standard background speckle (right). Between these extremes we can use fewer scatterers to represent underdeveloped speckle (middle). (b) Imaging targets for image-derived data, where the amplitude of each scatterer is weighted according to a grayscale image. This ground-truth contrast can be derived directly from the intensity of the image (left) or be first binarized (right) to emphasize anechoic regions. While all categories are used for the validation of the ML model, numerical experiments suggest that training on the class of data emphasized in red (ground truth contrast, underdeveloped speckle) produces the best optimized encoding sequences.

### 3. Results

#### 3.1. Optimization of Both Time Delays and Apodization Weights

We now demonstrate the capability of our proposed ML architecture to produce encoding sequences that meaningfully improve image quality. In the most general case, the available hardware allows us to manipulate both time delays and apodization weights for each array element, each up to some quantization. This allows the greatest freedom when designing encoding sequences, and predictably the greatest improvement over conventional sequences. As a prototypical configuration of the proposed ML architecture, we train the ML model using 400 simulated instances of the previously described underdeveloped speckle background with anechoic lesions, processed in batches of size 8. We evaluate the model with the  $\ell^2$  loss function in Equation 7 using an imaging target drawn from the ground truth echogenicity. The training is performed using the Adam optimizer using a learning rate of 0.1 over 25 epochs. During training, we restrict the space of encoding sequences  $\Sigma$  to those only realizable on the available Verasonics hardware (see Section 3.4). We note that a primary advantage of the proposed architecture is flexibility to the choice of imaging target and loss function, which can vary according to the needs of an application of interest. However, we will also see that the above configuration of the ML model produces an optimized encoding sequence that improves image quality fairly broadly across a number of different metrics.

We first demonstrate these improvements by evaluating the same optimized encoding sequence on several types of ultrasound data in Figure 3. These data include classical imaging scenarios featuring anechoic lesions or isolated point targets, where we observe significantly improved contrast and reduction of scattering artifacts respectively. For comparison, we use two conventional plane wave encodings of varying maximum angle extent, as such sequences characterize a common tradeoff between FOV and resolution at depth (Bottenus et al., 2023). For example, the first generates 15 beams with 1 degree of separation, which results in a higher resolution along a narrower FOV. This is particularly notable when imaging point targets, where some scatterers are essentially undetectable. By steering these 15 plane waves sufficiently far apart to cover the entire imaging domain, we are left with shallower contrast of anechoic regions owing to significant scattering of point targets throughout the domain. By contrast, our method has generated a sequence that can recover this wider FOV simultaneously with improved contrast even in the case of a severely underdetermined number of transmits.

To show that these improvements are a consequence of more general acoustic properties of the encoding sequence rather than over-specification to the training data, we demonstrate the same optimized sequence on the two other categories of image-derived data discussed in Section 2.4. In the first category the scatterers are weighted arbitrarily, and we see much finer detail near the edges of the domain and greater depth of anechoic regions. In the second category the scatterers are weighted uniformly with larger anechoic regions, and we see a degree of contrast comparable to conventional

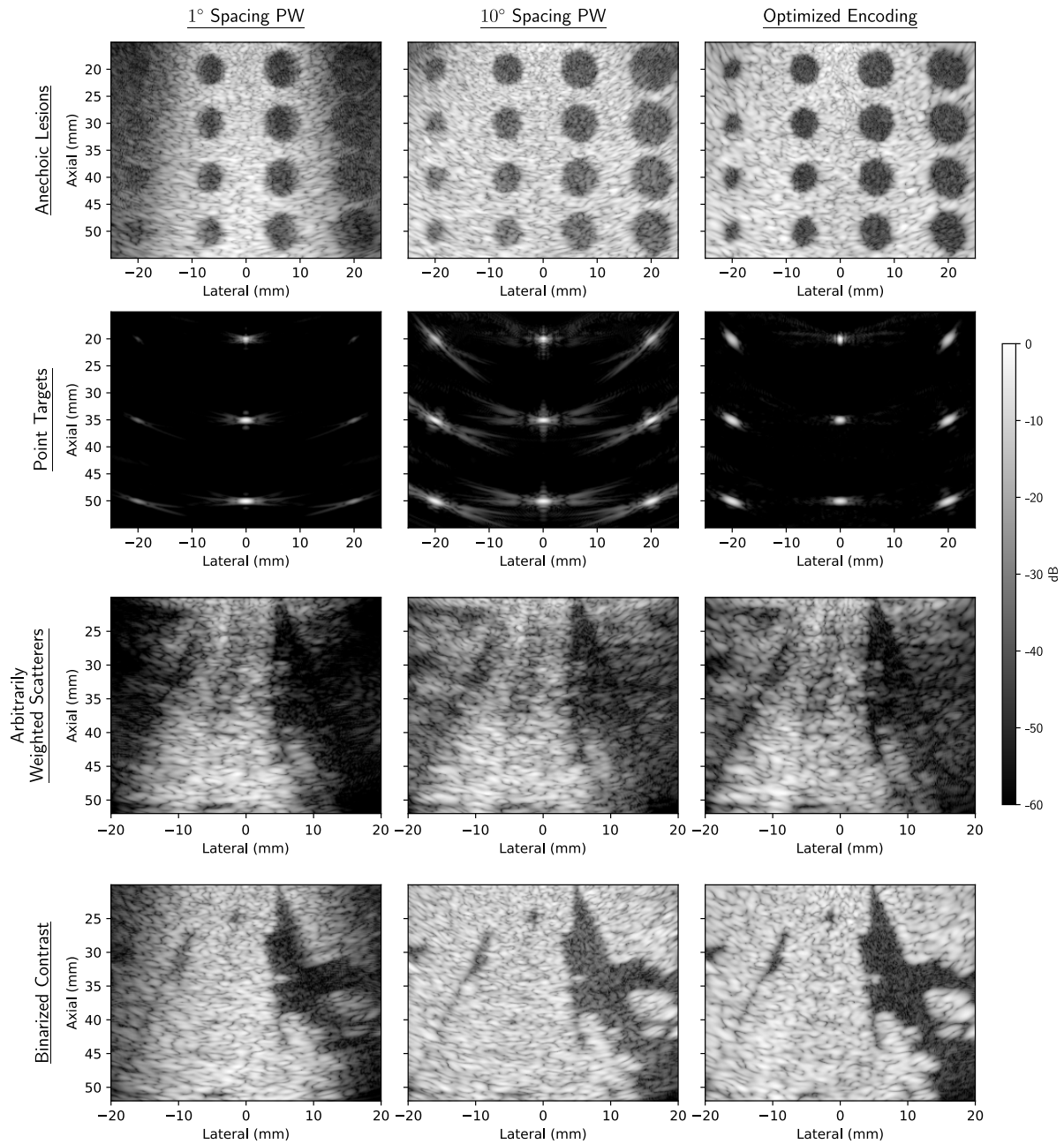


Figure 3: Three choices for 15-transmit encodings applied to different imaging targets. We compare the results of imaging with the REFoCUS framework using plane waves with 1 degree of separation (left), plane waves with 10 degrees of separation, which spans the whole imaging domain (middle), and our novel optimized sequence (right). We compare the results of imaging on classical targets, anechoic lesions and point targets, as well as our two categories of image derived data. In all cases, we see considerable improvements in contrast and resolution over the conventional transmit encodings.

circular cysts. Overall we also observe through Figure 3 that the benefits of the optimized encoding sequence are largely independent of the specific arrangement and amplitude of scatterers in the field. Instead, the optimized sequence improves the point spread function more fundamentally, and these improvements are consistent throughout the FOV of the image.

We show these improvements quantitatively in Table 2, where this prototypical optimized encoding sequence leads to improved  $\ell^2$  error against the ground truth echogenicity. Furthermore, we see that these improvements are maintained across several types of imaging targets. Notably, this is the same loss that is minimized over the training set (See Equation 7). We see that even though the ML model is exposed only to anechoic lesions in underdeveloped speckle during training, the quality as measured by this loss is improved among other image types that are visually quite distinct.

Average $\ell^2$ Loss against Ground Truth Contrast Map				
Target Type	1° Spacing Plane waves	Full FOV Span Plane waves	Truncated Hadamard	Optimized Encoding
Isolated Point Targets	12.55	20.03	33.87	<b>8.12</b>
Anechoic Lesions in Underdeveloped Speckle	583.9	331.6	366.3	<b>252.9</b>
Anechoic Lesions	530.8	250.5	257.3	<b>205.2</b>
Image-Derived Contrast	256.6	166.8	174.4	<b>160.8</b>
Binarized Image- Derived Contrast	369.9	258.8	274.7	<b>230.1</b>

Table 2: We compute the average  $\ell^2$  loss against the ground truth echogenicity across 50 pieces of simulated data outside the training set. Although the encoding sequence is trained using only the data set of anechoic lesions in underdeveloped speckle, this metric is also improved by our optimized encoding sequence over conventional sequences for each other type of data.

Furthermore, we can demonstrate that minimizing this  $\ell^2$  loss is strongly associated with improvements in more conventional image quality metrics. For example, the quality of the point spread function can be measured using the cystic resolution, which quantifies detectability of an anechoic cyst in background speckle with a given level of contrast (Ranganathan and Walker, 2007). While we can clearly see in Figure 4(b) that our optimized encoding sequence produces a low amount of scattering artifacts, the cystic resolution quantifies the concentration of energy around the point target. Similar to gCNR, such a metric is robust to artificial scaling of the dynamic range. By plotting the cystic contrast as a function of distance from the center in Figure 4(a),



we can measure the minimum radius of a cyst that can be detected with a contrast of  $-20$  dB using each of the above encoding sequences, where a smaller value indicates better focusing at the location of the point target. We observe that at the center of the imaging domain the optimized encoding sequence produces lesion detectability on par with narrowly concentrated plane waves.

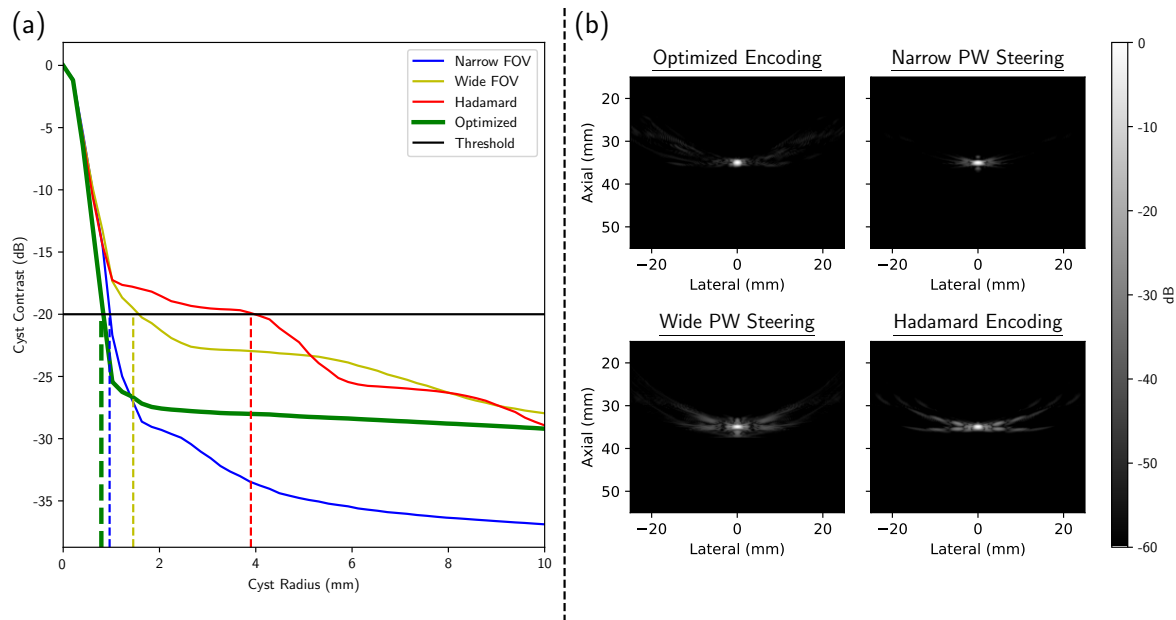


Figure 4: (a) The contrast of an anechoic cyst as a function of cyst size, with a vertical line indicating the cystic resolution, the minimum detectable cyst size with  $-20$  dB contrast. (b) The centered point targets for which the cystic resolution is measured. From this, we can see that the optimized encoding results in a minimum radius for detectability comparable to that of the narrow span plane waves.

In contrast to these narrow plane waves, however, our optimal encoding sequence is able to maintain this level of resolution throughout the imaging domain. To see this, we use Field II to simulate the responses from single, isolated scatterers distributed throughout the viewing window, and compute the cystic resolution for each. Shown in Figure 5, this procedure generates a map of lesion detectability measured through cystic resolution as a function of target position.

We also measure the overall cystic contrast using the gCNR. This metric also varies according to the spatial position of the lesion target. As such, we consider simulated anechoic lesion data of the kind in Figure 2(a), for which the position and radius of each lesion is random. We categorize these lesions based on position, and tabulate the average gCNR of lesions in each category in Figure 5. We can also measure the gCNR of the binarized, image-derived data of Figure 2(b). From this, we again see that our optimized encoding sequence outperforms conventional plane wave and Hadamard encodings in terms of both FOV and contrast.

We also compare our optimized sequence to standard techniques in apodization,

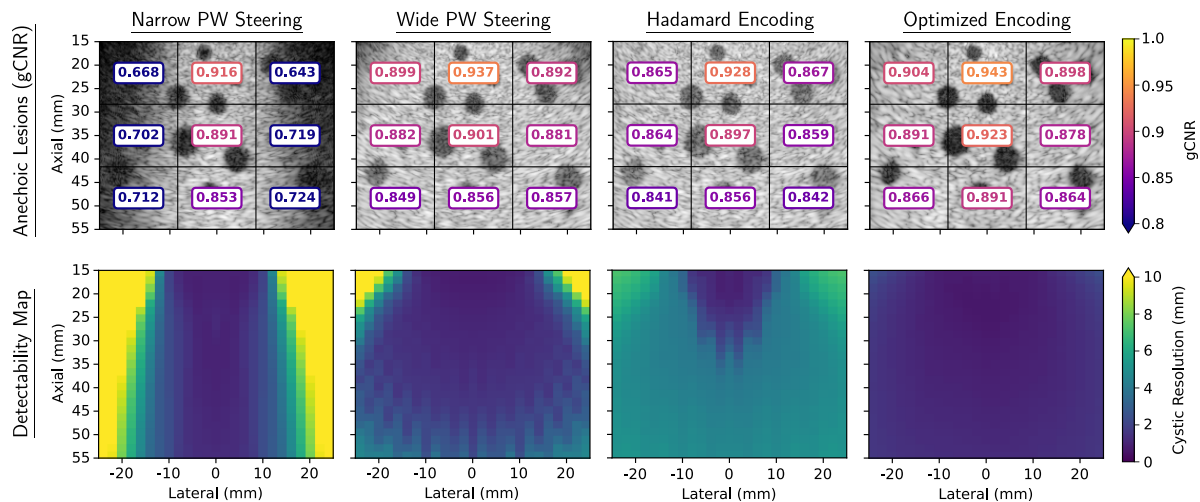


Figure 5: Quantitative improvements of optimized encoding sequence. (top) We plot the average gCNR for anechoic lesions in each region of the viewing range, averaged over randomly located targets over 50 instances of simulated data. These values are displayed on one sample from this simulated dataset, depicting one instance of randomly located targets. (bottom) We plot the cystic resolution throughout the domain, i.e. the minimum radius for lesion detectability with -20 dB of contrast. Observe that only our optimized encoding sequence is able to maintain the same quality measured by gCNR and cystic resolution throughout the imaging domain.

Average gCNR				
Target Type	1° Spacing Plane waves	Full FOV Span Plane waves	Truncated Hadamard	Optimized Encoding
Binarized Image-Derived Contrast	0.882	0.654	0.888	<b>0.891</b>

Table 3: We compute the average gCNR over 50 pieces of out-of-sample data whose ground truth contrast is derived from a grayscale image.

which similarly seek to improve the point spread function by reducing side lobes (Jeong and Kwon, 2020). To do this, we consider plane waves with  $10^\circ$  spacing, which offers the best of resolution at depth while imaging the full FOV of the conventional sequences considered, and apply a Tukey window to the receive channel. As expected, this causes a considerable improvement to cyst detectability in the image. However, there are still clear artifacts around the point scatterers themselves, as well as the same striation in the plots of cystic resolution as the unapodized case, all shown in Figure 6. These effects are not present in our optimized encoding sequence.

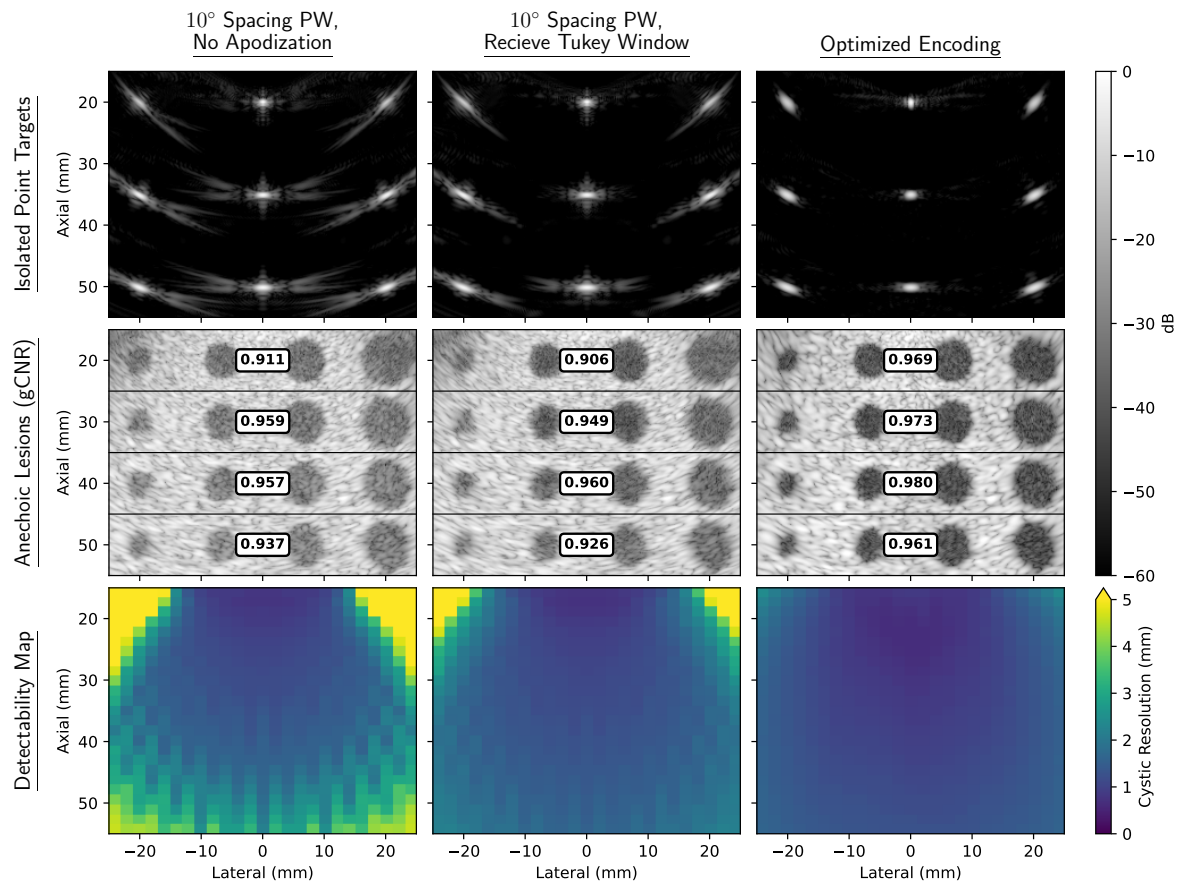


Figure 6: We compare our technique to a classical application of apodization applied to a plane wave configuration with  $10^\circ$  spacing. We do this visually (top), through the average gCNR across each row of lesions (middle) and the cystic resolution throughout the domain (bottom). In each case, we observe that although the Tukey window does improve the point spread function at the cost of some resolution as expected, these improvements are not as pronounced as those observed with our optimized sequence.

### 3.2. Restricted Optimization to Either Time Delays or Apodization Weights

We can also apply the provided framework for machine learning optimization to more restrictive hardware specifications. In doing so, we demonstrate that there is still considerable improvement present, although such sequences do not perform as well as a fully arbitrary system, as expected. To this end, we consider two relevant examples. In the first, the apodization weights are fixed to some uniform value, and the time delays are the *only* trainable parameters of the ML model. In the second, only the apodization weights can be changed, and each time delay is fixed as zero in the ML model. As in Section 3.1, we train the model on anechoic lesions in underdeveloped speckle and test the resulting sequence on data far outside the training set. We compare the resulting optimized sequence to the conventional alternative: wide spanning plane waves for delay-only optimization, and a truncated Hadamard encoding for weight-only optimization. These results of this comparison are compiled in Table 4. We see that in

each case the optimized sequence performs better according to the  $\ell^2$  loss metric than its conventional alternative, which we have now shown correlates with high quality as measured by gCNR and cystic resolution. Furthermore, we observe that while there is still considerable improvement when only delays are optimized through one of our ML models, the results of optimizing only weights is comparable to that of optimizing the full encoding sequence. This demonstrates that for our particular imaging scenario, optimization of the apodization weights has a more significant influence on the quality of the resulting sequence than delay optimization alone.

Average $\ell^2$ Loss against Ground Truth Contrast Map					
Target Type	Delay Optimization		Weight Optimization		Both
	Optimized	Full FOV Plane waves	Optimized	Truncated Hadamard	Optimized
Isolated Point Targets	<b>16.93</b>	20.03	<b>14.53</b>	33.87	<b>8.129</b>
Underdeveloped Speckle	<b>310.2</b>	331.6	<b>303.3</b>	366.3	<b>252.9</b>
Anechoic Lesions	<b>231.2</b>	250.5	<b>217.1</b>	257.3	<b>205.2</b>
Image-Derived Contrast	<b>165.7</b>	166.8	<b>164.2</b>	174.4	<b>160.8</b>
Binarized Image-Derived Contrast	<b>243.3</b>	258.8	<b>241.2</b>	274.7	<b>230.1</b>

Table 4: We consider optimizing each component of the encoding sequence, either only the delays or only the weights. While optimizing over delays, we keep the weights fixed to +1, making full FOV plane waves a meaningful comparison. While optimizing over weights, we keep the delays fixed to zero, making a truncated Hadamard code a meaningful comparison. In both cases, we see that the per-component optimized encoding sequence outperforms the conventional alternative on each type of imaging target, and in fact that quality of the weight-only optimization is comparable to that of the full sequence optimization.

### 3.3. Optimization in the Presence of Noise

These simulated results demonstrate the theoretical utility of applying an ML optimization strategy within the REFoCUS framework. However, we can verify that our optimized sequences produce meaningful improvements in more practical scenarios as well. In the first, we consider a separate configuration of the ML architecture that is tailored for an imaging system under the influence of electronic noise. During training, we model this by the addition of random noise to the encoded channel data prior to

imaging. We assume in this case that we have a known statistical model for this noise so that we may add realizations directly to our simulated training data. In the current example, this additive noise is sampled from a random normal distribution, filtered to have a bandwidth equal to that of the transducer, and then scaled to produce an average of 20 dB channel signal-to-noise ratio. It is in this context that restricting the set of apodization weights to an  $\ell^\infty$  ball is most critical, as otherwise all noise would be suppressed simply by increasing the apodization weights without bound.

By accounting for this noise model during training, the ML model generates a new encoding sequence that specifically acts to suppress this noise. We particularly see this in comparison to the optimized encoding sequence evaluated throughout Section 3.1. In Figure 7(a), we consider these two sequences, trained with and without the presence of noise, along with an additional plane wave configuration for comparison. We then apply each sequence to data to which noise is or is not added. In each of the four cases, there is considerable improvement over the conventional plane wave approach. However, we can also see that these improvements are most prominent when the ML model is trained with the same type of noise present during evaluation, the case emphasized in Figure 7(a) in red. In Figure 7(b), we consider a more complete evaluation of the case where noisy data is imaged using a sequence trained with the same noise model. There is the same degree of improvement as the noiseless case of Figure 3, featuring dramatic improvements in the gCNR and cystic resolution.

### 3.4. Experimental Verification

Finally, we verify these results directly by implementing an encoding sequence generated by our ML model in physical hardware. In particular, we implement the same encoding sequence evaluated on simulated data in Section 3.1. In the following experiments, we use the Verasonics Vantage 256 research scanner (Verasonics, Inc., Kirkland, WA) with the P4-2v phased array transducer (3 MHz transmit frequency, 64 elements, 0.3 mm pitch, 10V transmit voltage). Received channel data were stored for processing offline, where they were decoded and used to produce an image in the same manner as in the simulation. For comparison, we use sequences of 15 transmits that generate plane waves of varying span (15, 60, and 150 degrees). To reproduce the effects of arbitrarily scaled weights (rather than restricting to  $\pm 1$  through pulse inversion) we use the Verasonics apodization function to scale the duty cycle of the transmit excitation so that it matches the output amplitude. Although the system is limited to a minimum duty cycle of two clock cycles, which effectively nullifies low values for our weights, the optimized sequence was trained with this constraint accounted for in PyTorch by performing a projection onto this constraint set after each step of the optimization.

The first experiment utilizes an ATS 539 multi-purpose phantom (CIRS, Inc., Norfolk, VA) to confirm the ability of optimized encoding sequences to improve imaging on tissue-like material. Within the phantom we image anechoic lesions of varying position and radius in background speckle, and compute the gCNR of each with respect

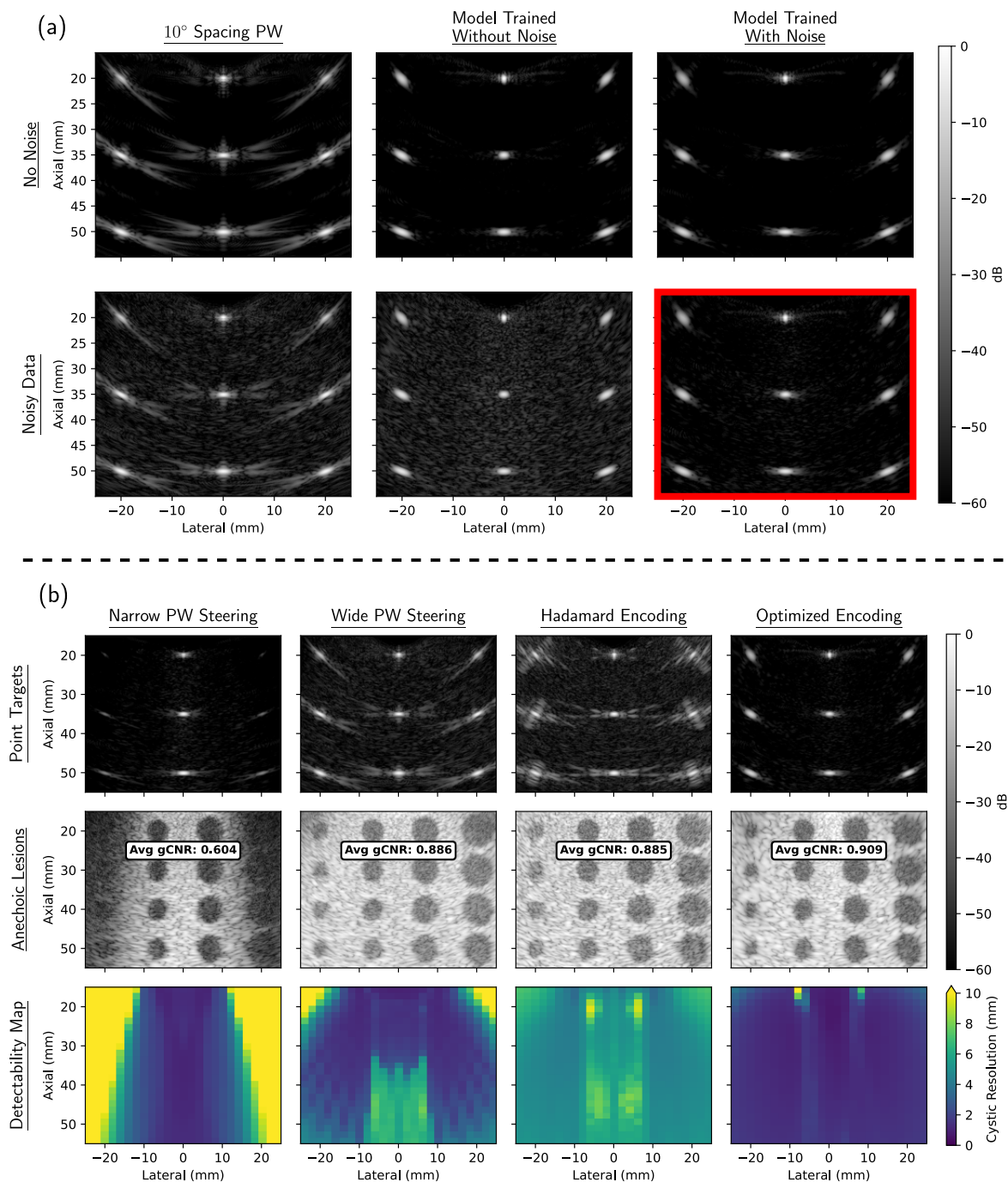


Figure 7: Effects of noise on training/evaluation of an ML model. (a) We compare encoding sequences generated by different ML models trained with and without the presence of electronic noise. In either training case there is considerable improvement over the conventional plane wave configuration (left), and these improvements are more pronounced when the encoding sequence is generated under the effects of the same noise model (right). (b) We make additional comparisons to the case emphasized in red in (a), comparing conventional transmit sequences on noisy RF data with an optimized sequence trained in the presence of additive noise. We see a greater qualitative suppression of noise (top), as well as improvements in gCNR (middle) and the point spread function as measured by the cystic resolution (bottom).

to surrounding background speckle. We show these gCNR values below each lesion in Figure 8(a). For a fixed lateral position, we acquire data using each encoding sequence at each of seven elevation positions of the phantom. In this way, we image anechoic lesions in the same positions with different realizations of background speckle, and compute the average gCNR across all realizations.

We can see that these results match closely with our numerical simulations, in that our optimized sequence is able to produce the depth of focus and resolution of a very narrow span of plane waves, while still maintaining a full FOV throughout the range. Importantly, these improvements persist beyond the fixed viewing window of the training data, which extends only to a depth of 55 mm. This further emphasizes that our encoding sequence has not simply specialized to the specific characteristics of the training data.

We can also recreate our simulated point target images, which we can in turn use to measure the cystic resolution throughout the imaging domain (albeit on a much coarser grid). To accomplish this, we image a custom, single target wire phantom (0.03 mm tungsten wire) in a water tank. Using the AIMS III Hydrophone Scanning System (Onda Corporation, Sunnyvale, CA), we mechanically translate the suspended P4-2v transducer around the fixed wire so that the target can be imaged from a  $6 \times 5$  grid of target positions ( $\sim 10$  mm lateral spacing,  $\sim 8$  mm axial spacing).

Although we only ever image one point target at a time with this experimental setup, in Figure 8(b), we present a *montage* of these images distributed appropriately in space. To ensure a fair visual comparison of each point target, we apply a *uniform* level of gain for each image in the domain. This allows us to very clearly see the effect of our optimized sequence on the FOV of the imaging system, where points in the upper corners of the viewing window are either undetectable or suffer from very poor resolution. In contrast, the optimized encoding sequence provides a uniform degree of resolution at all points in the domain.

Furthermore, we can see that the off-axis scattering artifacts present for each point target are greatly reduced when imaged with the optimized sequence. As before, we quantify this effect using the cystic resolution, which we can compute for each point target in Figure 8(b). Although our ability to perfectly capture this metric is slightly hampered by irregularities in the experimental setup, we still observe near uniform improvement over each conventional sequence, analogous to results observed in simulation.

#### 4. Discussion

As we have shown, our machine learning framework represents a novel method of generating transmit sequences that ultimately result in higher quality images than the standards currently in practice. However, as is the case in most machine learning applications, maximizing the efficacy of the optimized sequence requires careful consideration of the ML model configuration. For example, there are a number of

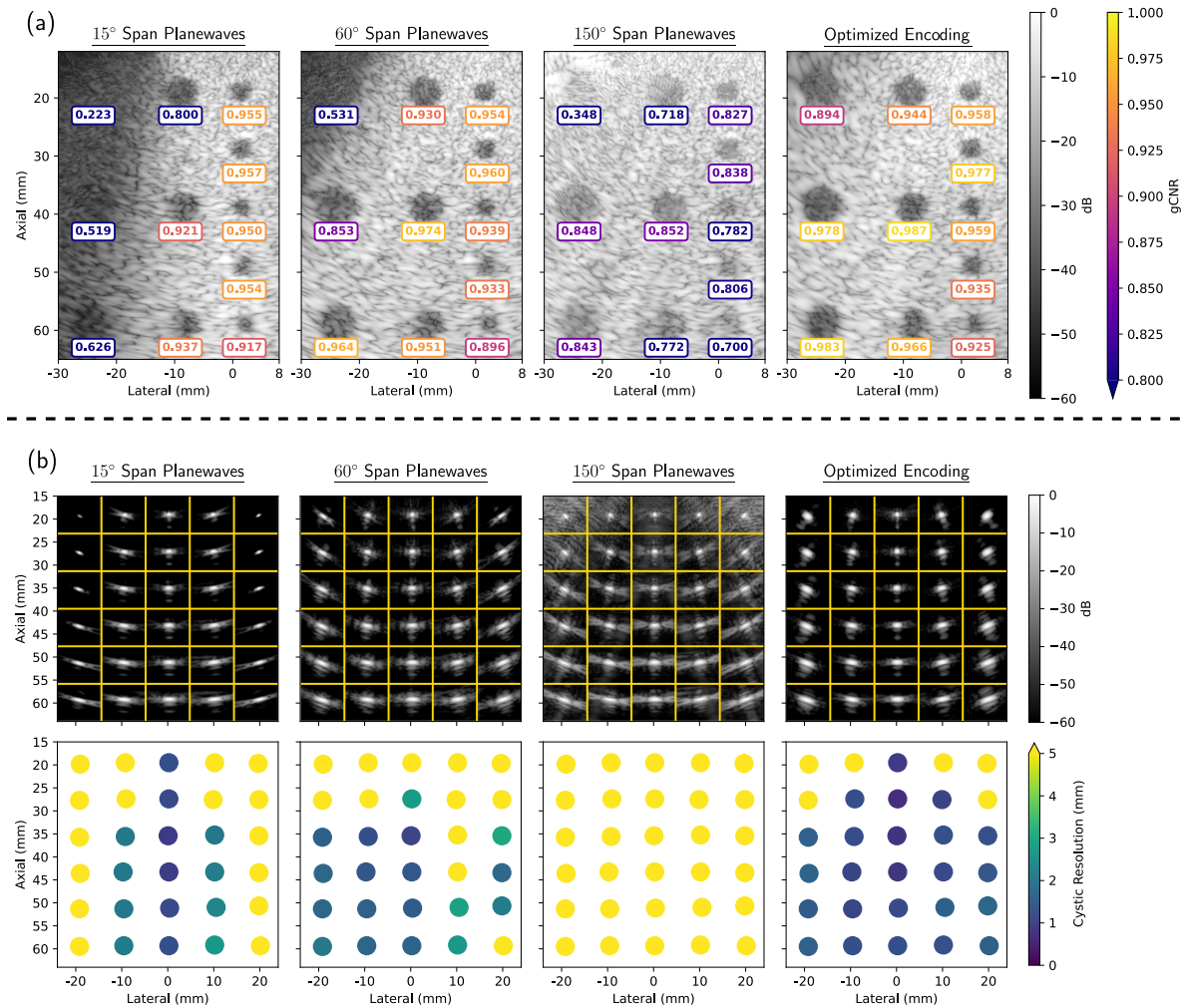


Figure 8: Experimental validation of simulated results. (a) We image the ATS 539 multi-purpose phantom using different encoding sequences. As in the simulated results, our optimized sequence improves image quality throughout and even beyond the viewing window of the training data. Although the ML model is optimized for a symmetric FOV, the fixed lateral position of the transducer was intentionally placed off-center to demonstrate improved FOV, while fully capturing each target in the asymmetric phantom. The average gCNR over seven realizations of the speckle pattern is shown beneath each anechoic lesion. (b) We create a montage of 30 individual point target images. Each is obtained by translating the P4-2v transducer around a fixed wire target in a water tank. To provide an appropriate comparison between different targets within the montage, each image is displayed with the same amount of gain (top). We use these images to compute the cystic resolution throughout the domain (bottom).



standard ML hyperparameters that must be selected, such as descent algorithm, batch size, learning rate, etc. However, this particular usage of an ML model in ultrasound brings about additional, unique considerations. In this section, we discuss our own exploration of these considerations, and make observations which we believe will be relevant in any future application that utilizes a beamformer as a component of an ML model for ultrasound imaging. In particular, we show that our ability to image a wide variety of targets with the same encoding sequence comes as a direct consequence of our choice of initial condition and training data.

#### 4.1. Significance of the Initial Condition and Training Data

Because the minimization problem presented in Equation 10 is not convex, there is no expectation that any optimization procedure would be able to find the global minimum. Furthermore, other features of the REFoCUS framework prevent this minimum from being unique, such as the inherent invariance to permutations of the transmissions. Instead, the particular local minimum approached by our optimization procedure is highly dependent on the initial condition. As the encoding sequences at these local minima can vary in quality, it is therefore important to select an initial condition that is anticipated to be at or near a good local minimum. Fortunately, the immediate interpretability of the parameters of our ML model provides a distinct advantage over conventional deep learning applications, as we can much more intelligently select this initial condition and analyze its effect.

As an example, a machine learning model initialized with a plane wave encoding will ultimately result in a set of transmissions that are steered in the same way, albeit with less well-defined wavefronts. On the other hand, initializing with a truncated Hadamard code causes the ML model to converge to a sequence with no immediately visible steering whatsoever. We can see these qualitative behaviors in Figure 9(a). Despite this, we have found experimentally that a truncated Hadamard sequence is a superior initial condition to a plane wave encoding, despite itself generally being a lower quality transmission sequence. This can be seen directly through the  $\ell^2$  loss plotted as a function of training epoch for each initial condition in Figure 9(b). This is because a truncated Hadamard sequence is in some sense quite general, as it allows the ML model to begin with near optimal FOV and both positive and negative apodization weights. Except for cases in which delays or weights must be fixed as in Section 3.2, each optimized encoding sequence used in this paper was generated by an ML model with this configuration as the initial condition.

In our exploration of this topic, we have found that recovering a known, conventional sequence is exceptionally difficult in all but the simplest of toy problems. For example, although plane wave encodings are generally quite performant, the ML model cannot identifiably recover the same geometric properties that make them desirable. On the other hand, the optimal qualities of the resulting sequence are quite opaque, suggesting that it would not be possible to discover them *without* the use of such an ML model.

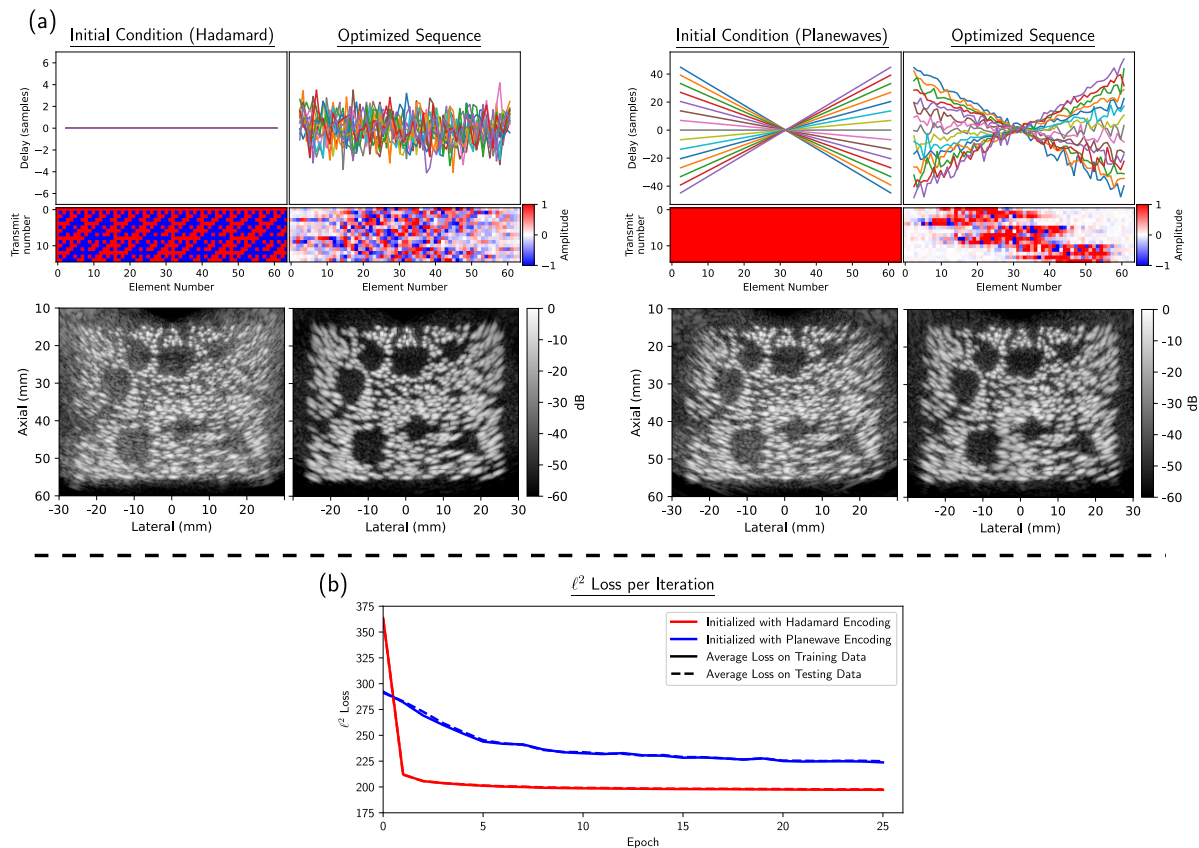


Figure 9: A comparison between two different encoding sequences used as initial conditions, a truncated Hadamard encoding and a wide FOV plane wave encoding. (a) For each initial condition, we plot the transmit sequence before and after optimization, along with one piece of testing data for each. In the delay plots, each transmission is represented by a single line. (b) For each initial condition, we plot the  $\ell^2$  loss function averaged over the training and testing data sets at each epoch. We note that although the initial plane wave encoding is a more effective sequence than the initial truncated Hadamard encoding, the optimization procedure finds a more optimal local minima when initialized with the latter. Furthermore, we note that the two curves are in near perfect agreement for each initial condition, indicating that our ML model has fully captured inherent acoustic properties of the transmit sequence that make it optimal for imaging, i.e. the point spread function.

Notably, we also observe in Figure 9(b) that in either case of initialization, our machine learning model performs nearly identically between our training and testing data. This is a highly desired property in this context, as ultrasound imaging can be theoretically formulated as a convolution of a spatially varying point spread function across each scatterer in the domain, the results of which are then summed to form an image. As a result of this, an effective manner of optimizing image quality for arbitrary data is to optimize this point spread function itself, concentrating it at the origin. Although our loss function does reference features of the point spread function directly, our choice to use underdeveloped speckle as training data implicitly encourages this type of improvement. An important feature of this particular class of training

data is that the scatterers within each sample are sparse enough that their off-axis scattering artifacts do not necessarily overlap one another, as is would be the case with standard background speckle. This means the  $\ell^2$  loss function can only be meaningfully decreased by concentrating the energy of each scatterer inwards, thereby improving the point spread function. On the other hand, scatterers among *all* samples in the training data are densely distributed throughout the imaging domain. This means that learning improvements that span the entire FOV can be obtained with relatively few samples of this particular kind of training data.

#### 4.2. Significance of the Imaging Target

Although we have restricted our ML architecture to loss functions that compare the resulting B-mode image directly to some ground truth imaging target, there is still a large amount of flexibility in that choice. As discussed in Section 2.2, the two most natural choices for target are images generated from the ground truth multistatic data or images generated from the ground truth echogenicity. While the two approaches are similar conceptually, we have found that the latter comparison is near universally superior in terms of resultant image quality. This is in some sense intuitive, as DAS beamforming applied to the unencoded multistatic data does not produce an optimal point spread function, evidenced by the presence of strong side lobes on point targets throughout the domain. When the ML model is trained on such images, it will be encouraged to replicate these side lobes, which is generally undesirable. We compare the two types of imaging targets in Figure 10, and see that by training against the exact ground truth, the resulting image has an improved point spread function.

As another example, we refer to the discussion in Section 2.4, where we “pad” images of underdeveloped speckle beyond the viewing window so that the background speckle itself is located in an anechoic field. While unintuitive, this ensures that the encoding sequence is not unnecessarily dependent on the specific domain geometry. The consequences of this are best seen through the following plots of cystic resolution in Figure 11, where the first encoding sequence is trained on images whose extent is exactly that of the final viewing window. In contrast, the second encoding sequence is trained on images located in a slightly wider anechoic void. As we can see, failure to add this empty space results in point spread functions that are the same nearly everywhere, save for two very prominent artifacts in the center of the region. In effect, these streaks depict positions at which common scattering artifacts extends beyond the imaging domain, and the incurred error is therefore not captured by the loss function.

## 5. Conclusions

In summary, we have shown that the principles of machine learning can be applied within the context of the REFoCUS model to generate encoding sequences that improve the quality of ultrasound imaging. By using novel advances in differentiable beamforming,

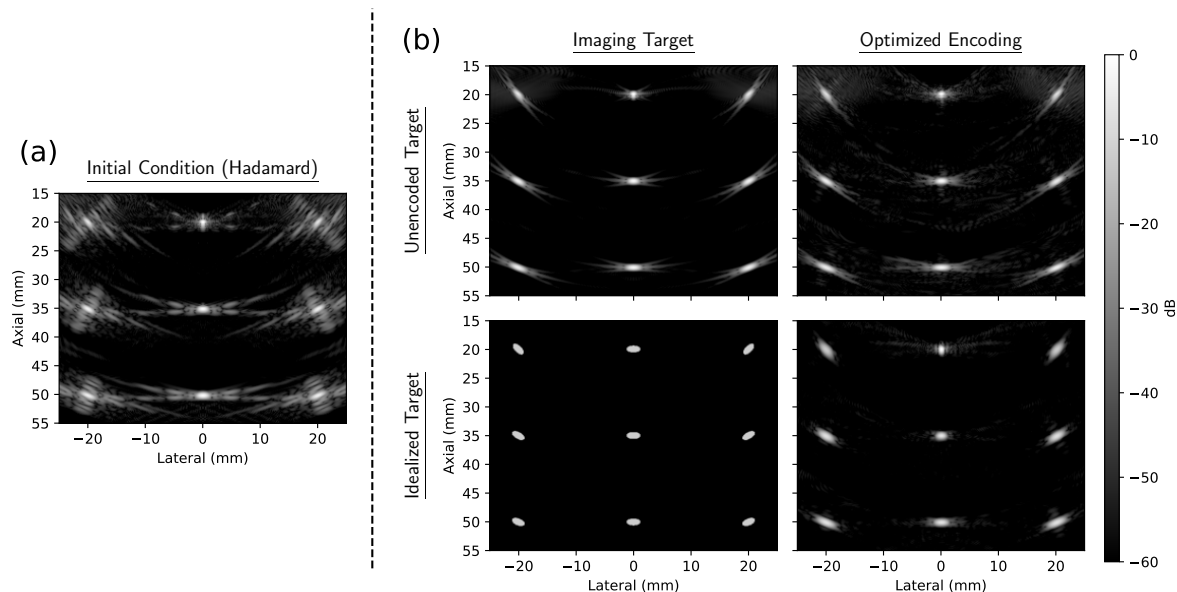


Figure 10: The quality of the encoding sequence depends heavily on the imaging target used during training. (a) We initialize two ML models identically. (b) When the imaging target of the  $\ell^2$  loss is unencoded data (top), the resulting sequence has the same artifacts present in the beamformed image. By using an idealized imaging target, i.e., one that represents the ground truth contrast, the resulting sequence can suppress these artifacts (bottom).

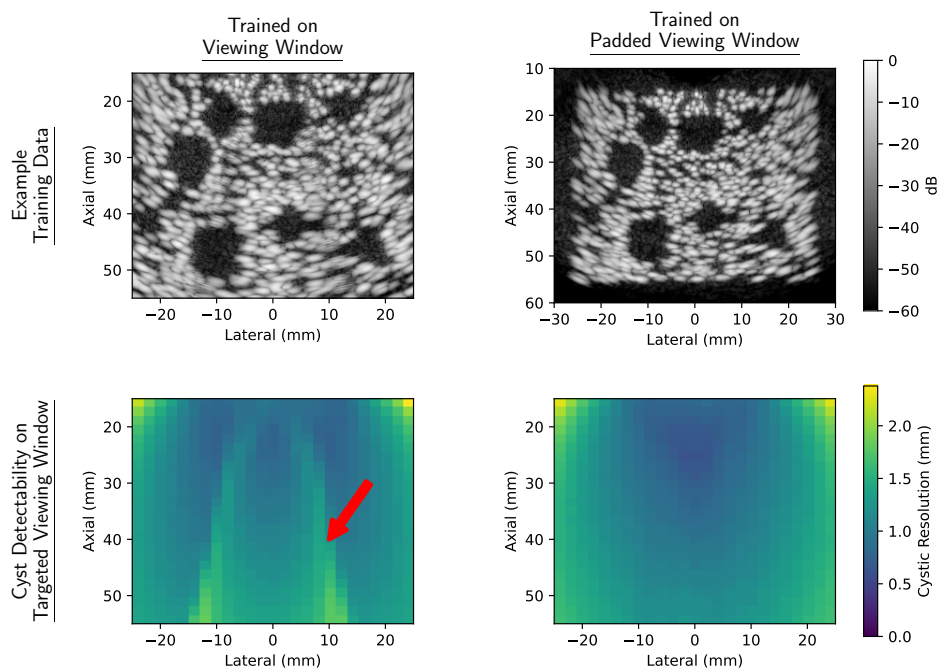


Figure 11: The imaging target must be carefully selected to ensure there is not an unnecessary dependence on the specifics of the imaging domain. For example, by expanding the window during training (right), we are able to deal with streaking artifacts (indicated with an arrow) that arise from unsuppressed scattering just beyond the imaging domain.

we are able to update the parameters of our ML model according to improvements in an *imaging* metric, a novel departure from existing work that only considers the recovery of the multistatic data set. An important consequence of this is that in doing so we can demonstrate the existence of transmit sequences that produce images with higher resolution and contrast, yet the encoding itself produces a *worse* reconstruction of  $\mathbf{u}$  from  $\mathcal{S}$ . This is in some sense unsurprising, as even a perfect reconstruction of  $\mathbf{u}$  will only produce the original, *unencoded* image. Yet as seen in Figure 10, this type of imaging target inherently lacks many desirable properties. To create a concrete example of this phenomenon, we compare to an ML model within our framework that is instead configured to directly optimize the recovery of the multistatic data set by minimizing

$$\mathcal{L}_{\text{STA}}(\hat{\mathbf{u}}; \mathbf{u}) := \frac{1}{N_T N_R N_\omega} \|\mathbf{u} - \hat{\mathbf{u}}\|_2^2. \quad (11)$$

We see that this new configuration successfully generates an encoding sequence that produces a lower STA loss than the previously defined encoding sequence optimized for image recovery. Yet despite this numerical improvement, we see in Figure 12 that there is a clear superiority in image quality when the optimization process takes image formation into consideration, bringing about improvements both visually and in terms of the gCNR averaged over each lesion. Furthermore, we take this as a counterexample to the common convention that better conditioning of the encoding matrices  $\mathcal{H}$  necessarily corresponds to higher quality images. To account for the effects of Tikhonov regularization, we measure this condition number as  $\kappa = \|\mathcal{H}_0\| \cdot \|\mathcal{H}_0^\dagger\|$ , doing so because the encoding matrix for the largest frequency  $\mathbf{H}(0)$  has the poorest conditioning among the collection  $\mathcal{H}$ . We see that both encoding sequences bring about reasonably well-conditioned matrices following Tikhonov regularization, with the sequence optimized for data recovery even having a slightly improved value of  $\kappa$ . However, there are still clear qualitative differences between the two images.

An important theoretical consequence of the proposed ML architecture is its ability to discover currently unknown transmit sequences with desirable properties. For example, the various ML models used throughout this paper have found transmit sequences that are each “high-quality” in a sense that is acoustically meaningful, yet does not follow directly from the training procedure. That is to say, although the sequence is selected so that it minimizes one particular  $\ell^2$  imaging metric, it ultimately improves quality along a number of other metrics across (from the perspective of this imaging loss) disparate classes of data. At the same time, the exact acoustic properties that these sequences share is as of yet obscure. This means that our ML model has stumbled upon a currently unexplored regime of transmit sequences, and there remain unanswered questions as to the characteristics of such sequences.

The inherent flexibility of the proposed ML architecture, whose parameters are exactly those of an encoding sequence, has important practical consequences. Compared to approaches in deep learning, there are very few trainable parameters, particularly in the cases of interest with an underdetermined number of transmits. While we have

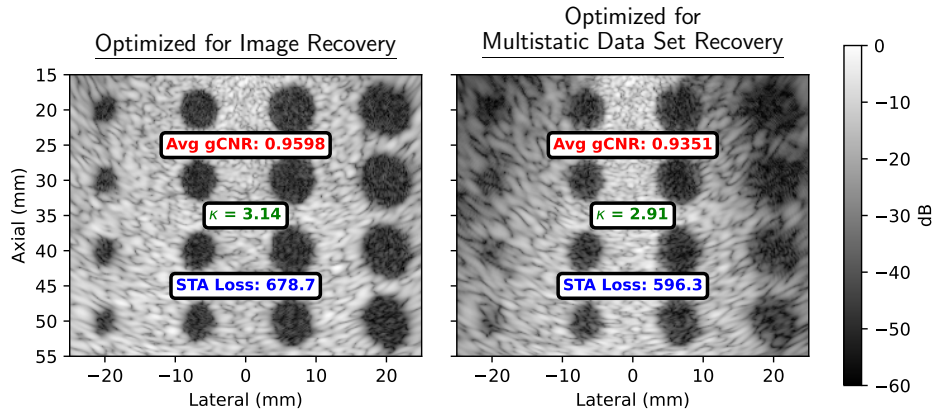


Figure 12: Comparison of our optimized sequence to one that is trained to optimize reconstruction of the multistatic data set. In spite of a worse multistatic reconstruction measured by the STA loss and comparable condition number  $\kappa$  for the encoding matrices, our strategy for optimization produces visibly improved contrast and resolution throughout the image.

shown that our particular configuration of training data and loss function generalizes well to a wide range of classical imaging scenarios, one can easily adapt the ML architecture to other imaging tasks, such as the above usage that instead minimizes STA recovery. Because the model can be trained very quickly for each configuration, the model can be designed even for a very narrow imaging scope, such as a different viewing window or beamforming parameters.

Furthermore, the high degree of generalizability shown in Figure 3 indicate that, in sharp contrast to other deep-learning image formation and analysis tasks, it may be possible to train with a limited amount of *in vivo* data without a severe degradation in model quality. Altogether, the theoretical generality of the REFoCUS framework is a key component of this type of investigation, as it allows for uniform treatment of highly variable kinds of transmit sequences. In future work, we wish to further explore the capabilities of machine learning within REFoCUS, motivated by our ability to incorporate beamforming as a layer of the ML architecture, potentially with its own set of trainable parameters. As has been the case in this work, such technology will ultimately allow us to continue to develop techniques that directly improve image quality for applications of interest.

## References

- Ali R, Herickhoff C D, Hyun D, Dahl J J and Bottenus N 2020 IEEE Transactions on Ultrasonics, Ferroelectrics, and Frequency Control **67**(5), 943–956.
- Bottenus N 2018 IEEE Transactions on Ultrasonics, Ferroelectrics, and Frequency Control **65**(1), 30–38.

- Bottenus N, Spainhour J and Becker S 2023 IEEE Transactions on Ultrasonics, Ferroelectrics, and Frequency Control **70**(1), 52–63.
- Chen Y, Liu J, Luo X and Luo J 2021 IEEE Transactions on Medical Imaging **40**(11), 3190–3204.
- Chiao R, Thomas L and Silverstein S 1997 1997 IEEE Ultrasonics Symposium pp. 1679–1682.
- Claerbout J 2014 Geophysical image estimation by example LULU COM.
- Cobbold R S C 2007 Foundations of Biomedical Ultrasound Biomedical Engineering Series Oxford University Press.
- Dei K, Luchies A and Byram B 2017 in ‘2017 IEEE International Ultrasonics Symposium (IUS)’ pp. 1–4.
- Griewank A and Walther A 2008 Evaluating Derivatives second edn Society for Industrial and Applied Mathematics.  
**URL:** <https://epubs.siam.org/doi/abs/10.1137/1.9780898717761>
- Harrison T, Samplaleanu A and Zemp R 2014 IEEE Transactions on Ultrasonics, Ferroelectrics, and Frequency Control **61**(5), 886–890.
- Howard A, Park E and Kan W 2018 ‘Imagenet object localization challenge’.  
**URL:** <https://kaggle.com/competitions/imagenet-object-localization-challenge>
- Hyun D 2022 in S Aylward, J. A Noble, Y Hu, S.-L Lee, Z Baum and Z Min, eds, ‘Simplifying Medical Ultrasound’ Springer International Publishing Cham pp. 128–138.
- Hyun D, Brickson L L, Looby K T and Dahl J J 2019 IEEE Transactions on Ultrasonics, Ferroelectrics, and Frequency Control **66**(5), 898–910.
- Hyun D, Wiacek A, Goudarzi S, Rothlübbers S, Asif A, Eickel K, Eldar Y C, Huang J, Mischi M, Rivaz H, Sinden D, van Sloun R J G, Strohm H and Bell M A L 2021 IEEE Transactions on Ultrasonics, Ferroelectrics, and Frequency Control **68**(12), 3466–3483.
- Jensen J A 1996 Medical & Biological Engineering & Computing **34**(Supplement 1, Part 1), pp. 351–353.
- Jensen J A, Nikolov S I, Gammelmark K L and Pedersen M H 2006 Ultrasonics **44**, e5–e15.
- Jeong M K and Kwon S J 2020 Ultrasonography **40**, 289 – 300.  
**URL:** <https://api.semanticscholar.org/CorpusID:221347862>
- Kingma D P and Ba J 2017 ‘Adam: A method for stochastic optimization’.
- Krizhevsky A, Sutskever I and Hinton G E 2017 Commun. ACM **60**(6), 84–90.  
**URL:** <https://doi.org/10.1145/3065386>
- Liu S, Wang Y, Yang X, Lei B, Liu L, Li S X, Ni D and Wang T 2019 Engineering **5**(2), 261–275.  
**URL:** <https://www.sciencedirect.com/science/article/pii/S2095809918301887>

- Long W, Bottenus N and Trahey G E 2018 IEEE Transactions on Ultrasonics, Ferroelectrics, and Frequency Control **65**(10), 1768–1780.
- Mischi M, Lediju Bell M A, van Sloun R J G and Eldar Y C 2020 IEEE Transactions on Ultrasonics, Ferroelectrics, and Frequency Control **67**(12), 2477–2480.
- Noda T, Tomii N, Nakagawa K, Azuma T and Sakuma I 2020 IEEE Transactions on Ultrasonics, Ferroelectrics, and Frequency Control **PP**, 1–1.
- Paszke A, Gross S, Massa F, Lerer A, Bradbury J, Chanan G, Killeen T, Lin Z, Gimelshein N, Antiga L, Desmaison A, Köpf A, Yang E, DeVito Z, Raison M, Tejani A, Chilamkurthy S, Steiner B, Fang L, Bai J and Chintala S 2019 ‘Pytorch: An imperative style, high-performance deep learning library’.
- Perrot V, Polichetti M, Varray F and Garcia D 2021 Ultrasonics **111**, 106309.
- Ranganathan K and Walker W F 2007 IEEE Transactions on Ultrasonics, Ferroelectrics, and Frequency Control **54**(4), 782–792.
- Rodriguez-Molares A, Marius O, Rindal H and Jan D 2019 IEEE Transactions on Ultrasonics, Ferroelectrics, and Frequency Control pp. 1–12.
- Spainhour J, Becker S and Bottenus N 2022 in ‘2022 IEEE International Ultrasonics Symposium (IUS)’ pp. 1–4.
- van Sloun R J G, Cohen R and Eldar Y C 2020 Proceedings of the IEEE **108**(1), 11–29.
- You Q, Dong Z, Lowerison M R and Song P 2021 IEEE Transactions on Ultrasonics, Ferroelectrics, and Frequency Control pp. 1–1.
- Zhang J, Liu J, Fan W, Qiu W and Luo J 2022 Physics in Medicine & Biology **67**(10), 1–18.